# Electronic Supplementary Information for:

# Resonant doping for high mobility transparent conductors: the case of Mo-doped $In_2O_3$

Jack E. N. Swallow[1], Benjamin A. D. Williamson[2,3], Sanjayan Sathasivam[2], Max Birkett[1], Thomas J. Featherstone[1], Philip A. E. Murgatroyd[1], Holly J. Edwards[1], Zachary W. Lebens-Higgins[4], David A. Duncan[5], Mark Farnworth[6], Paul Warren[6], Nianhua Peng[7], Tien-Lin Lee[5], Louis F. J. Piper[4], Anna Regoutz[2], Claire J. Carmalt[2], Ivan P. Parkin[2], Vin R. Dhanak[1], David O. Scanlon[2,3,5*] & Tim D. Veal[1*]

[1]*Stephenson Institute for Renewable Energy and Department of Physics, University of Liverpool, Liverpool L69 7ZF, UK*

[2]*Department of Chemistry, University College London, 20 Gordon Street, London WC1H 0AJ, UK*

[3]*Thomas Young Centre, University College London, Gower Street, London WC1E 6BT, UK*

[4]*Department of Materials Science and Engineering, Binghamton University, Binghamton, New York 13902, USA*

[5]*Diamond Light Source, Didcot, Oxfordshire OX11 0DE, UK*

[6]*NSG Group, European Technical Centre Hall Lane, Lathom, Ormskirk, Lancashire L40 5UF, UK*

[7]*Surrey Ion Beam Centre, University of Surrey, Surrey, GU2 7XH, UK*

**e-mail: D.Scanlon@ucl.ac.uk; T.Veal@liverpool.ac.uk*

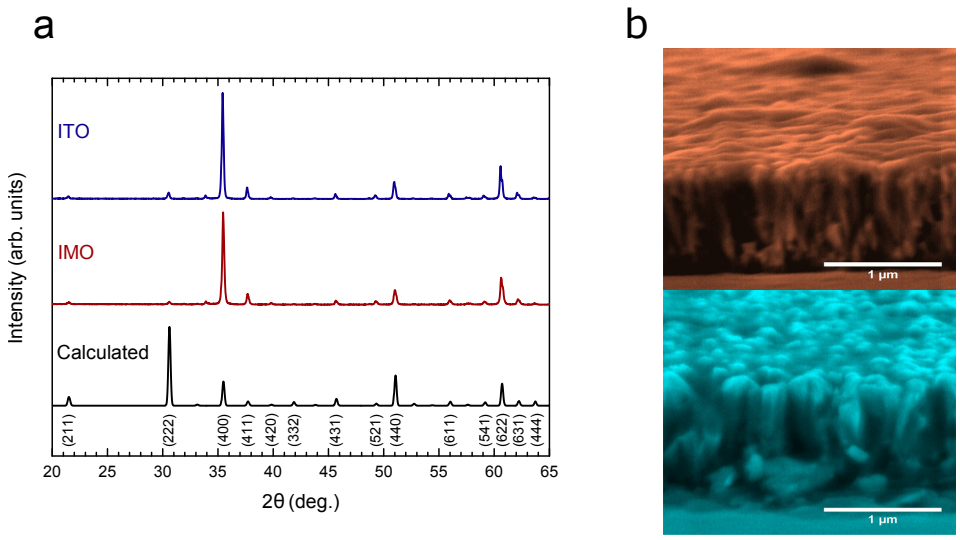


Fig. S1: **a** X-ray diffraction patterns of ITO and IMO and **b** typical cross-sectional SEM image for both IMO (top) and ITO (bottom), used to determine film thickness for the range of films in this study.

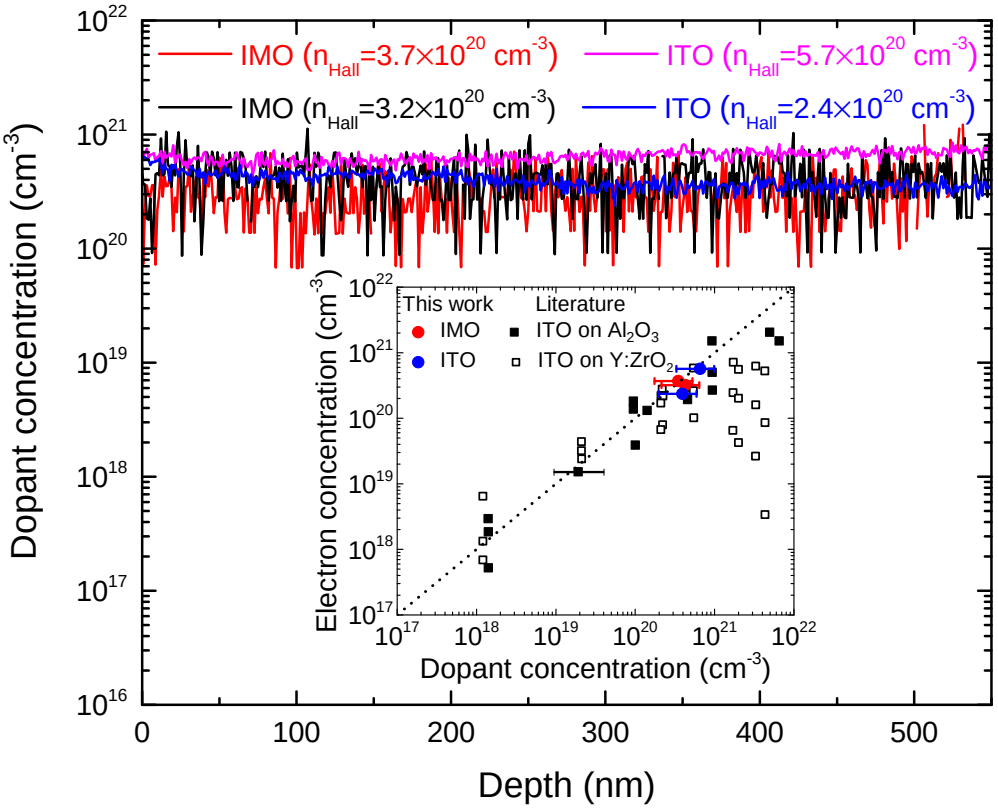


Fig. S2: Dopant concentration versus depth for IMO and ITO films determined by secondary ion mass spectrometry. The Mo and Sn concentrations are calibrated using Mo and Sn ion implanted standards. The inset shows the dopant concentration from SIMS versus electron concentration from Hall effect measurement for our IMO (red) and ITO films (blue). This indicates that, to within the measurement uncertainty, there is one electron per dopant atom. Previously published data on ITO films is also shown for comparison.[1]

Table S1: Important physical parameters for the series of IMO and ITO films used in this study. These are carrier density ($n$), free carrier mobility ($\mu$), resistivity ($\rho$) and sheet resistance ($R_S$) as determined by four point probe and Hall effect measurements, thickness ($d$) as determined by cross sectional SEM and confirmed by IR reflectivity modelling, optical transmission at 550nm ($T_{550}$), the Haacke figure of merit ($\Phi_H$) determined from $R_S$ and the optical transmission at $\lambda = 550$nm, and the plasma frequency from infrared reflection measurements and modelling.

| | $n$ | $\mu$ | $\rho$ | $R_S$ | d | $T_{550}$ | $\Phi_H$ | $\omega_p$ |
|---|---|---|---|---|---|---|---|---|
| | ($10^{20}$cm$^{-3}$) | (cm$^2$V$^{-1}$s$^{-1}$) | ($10^{-4}\Omega$ cm) | ($\Omega/\square$) | (nm) | (%) | ($10^{-3}\Omega^{-1}$) | (eV) |
| IMO | 2.2 | 94.8 | 3.0 | 3.7 | 800 | 73.6 | 12.6 | 0.51 |
| | 3.2 | 110.8 | 1.8 | 2.3 | 750 | 72.2 | 16.7 | 0.63 |
| | 3.7 | 122.7 | 1.4 | 2.1 | 670 | 69.9 | 13.3 | 0.65 |
| | 5.0 | 107.3 | 1.2 | 1.7 | 700 | 67.7 | 12.0 | 0.69 |
| | 4.1 | 99.4 | 1.5 | 2.3 | 670 | 52.4 | 0.8 | 0.71 |
| ITO | 2.4 | 52.0 | 5.1 | 3.2 | 1600 | 57.7 | 1.3 | 0.61 |
| | 7.0 | 29.5 | 3.1 | 2.8 | 1100 | 54.6 | 0.8 | 0.82 |
| | 5.7 | 28.9 | 3.8 | 2.4 | 1600 | 51.9 | 0.6 | 0.70 |
| | 6.3 | 31.5 | 3.1 | 2.4 | 1300 | 59.5 | 2.3 | 0.82 |
| | 8.3 | 16.0 | 4.7 | 3.9 | 1200 | 62.8 | 2.5 | 0.87 |
| | 10.7 | 9.2 | 6.3 | 7.0 | 900 | 66.0 | 2.2 | 0.93 |
| | 11.5 | 16.4 | 3.3 | 3.7 | 900 | 68.8 | 6.4 | 0.93 |
| | 5.4 | 24.7 | 4.7 | 6.7 | 700 | 75.6 | 9.1 | 0.68 |

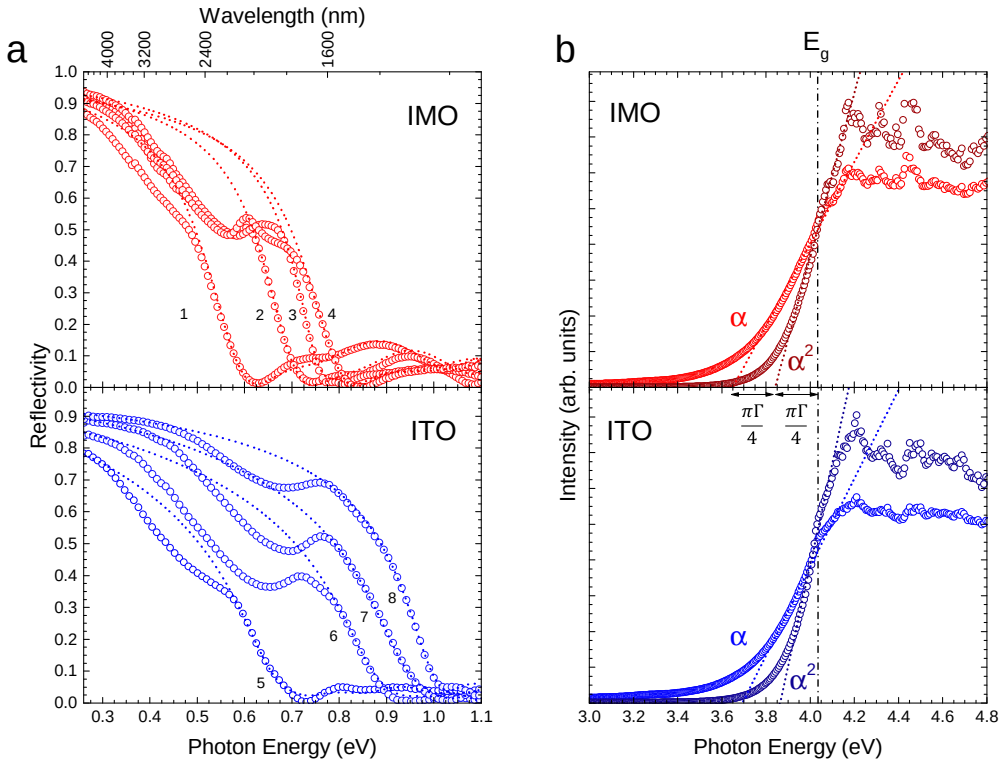


Fig. S3: Optical measurements and data extraction methods. **a.** Infrared-reflectivity measurements as a function of photon energy for both IMO and ITO films with a range of carrier densities: (1) $2.23\times10^{20}$ cm$^{-3}$, (2) $3.20\times10^{20}$ cm$^{-3}$, (3) $5.02\times10^{20}$ cm$^{-3}$, (4) $4.14\times10^{20}$ cm$^{-3}$, (5) $2.36\times10^{20}$ cm$^{-3}$, (6) $6.94\times10^{20}$ cm$^{-3}$, (7) $8.29\times10^{20}$ cm$^{-3}$, (8) $1.07\times10^{21}$ cm$^{-3}$. Dotted lines represent model fit curves used to extract the film plasma frequency. A dip in each of the spectra compared with the model curves is associated with surface roughness. **b.** Typical absorption spectra for IMO (n=$4.14\times10^{20}$cm$^{-3}$) and ITO (n=$6.94\times10^{20}$cm$^{-3}$) films. The displayed data sets exhibit similar energy gaps but very different carrier densities. Both the absorption coefficient $\alpha$ and $\alpha^2$ are plotted and the optical gaps extracted using the methods originally derived by Hamberg et al.[2], illustrated by Dolgonos et al.[3]

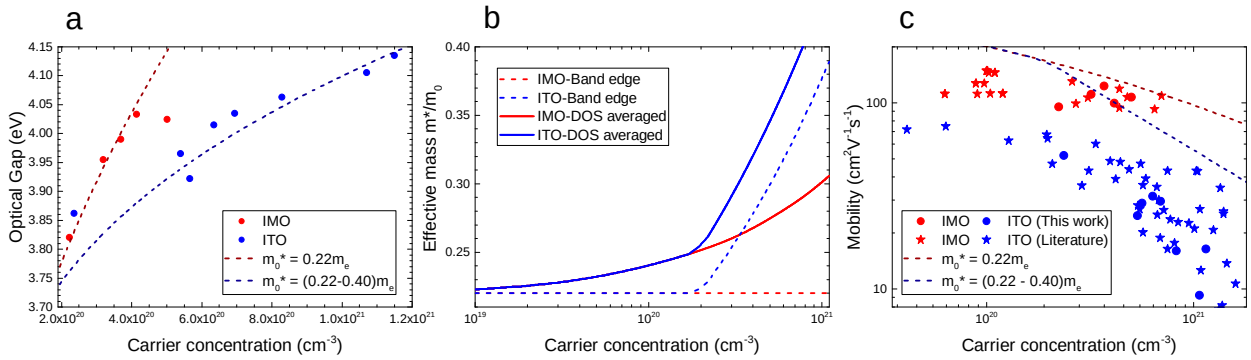


Fig. S4: **a** Optical gap as a function of carrier density for IMO and ITO films. The model curves are shown as dashed lines, and are calculated in the same way as that for Main Fig. 2b using equation 3. **b** Calculated band edge and density-of-states averaged effective masses for IMO and ITO. The ITO values deviate from those of IMO at $2 \times 10^{20}$ cm$^{-3}$ as this is the lowest carrier density of ITO studied here. We expect that a smooth transition to occur between IMO and ITO values will occur in the $10^{19}$ cm$^{-3}$ carrier density range as the Sn concentration increases and the mixing between Sn 5$s$ and CBM states increases. **c** Mobility as a function of carrier density. Measurements presented from this work are displayed as circles whilst data taken from the literature for IMO[4–9] and ITO [5,10–15] samples deposited via various methods are stars. Model curves are calculated using the degenerate form of the Brooks-Herring model for ionized impurity scattering, taking into account conduction band non-parabolicity[16,17].

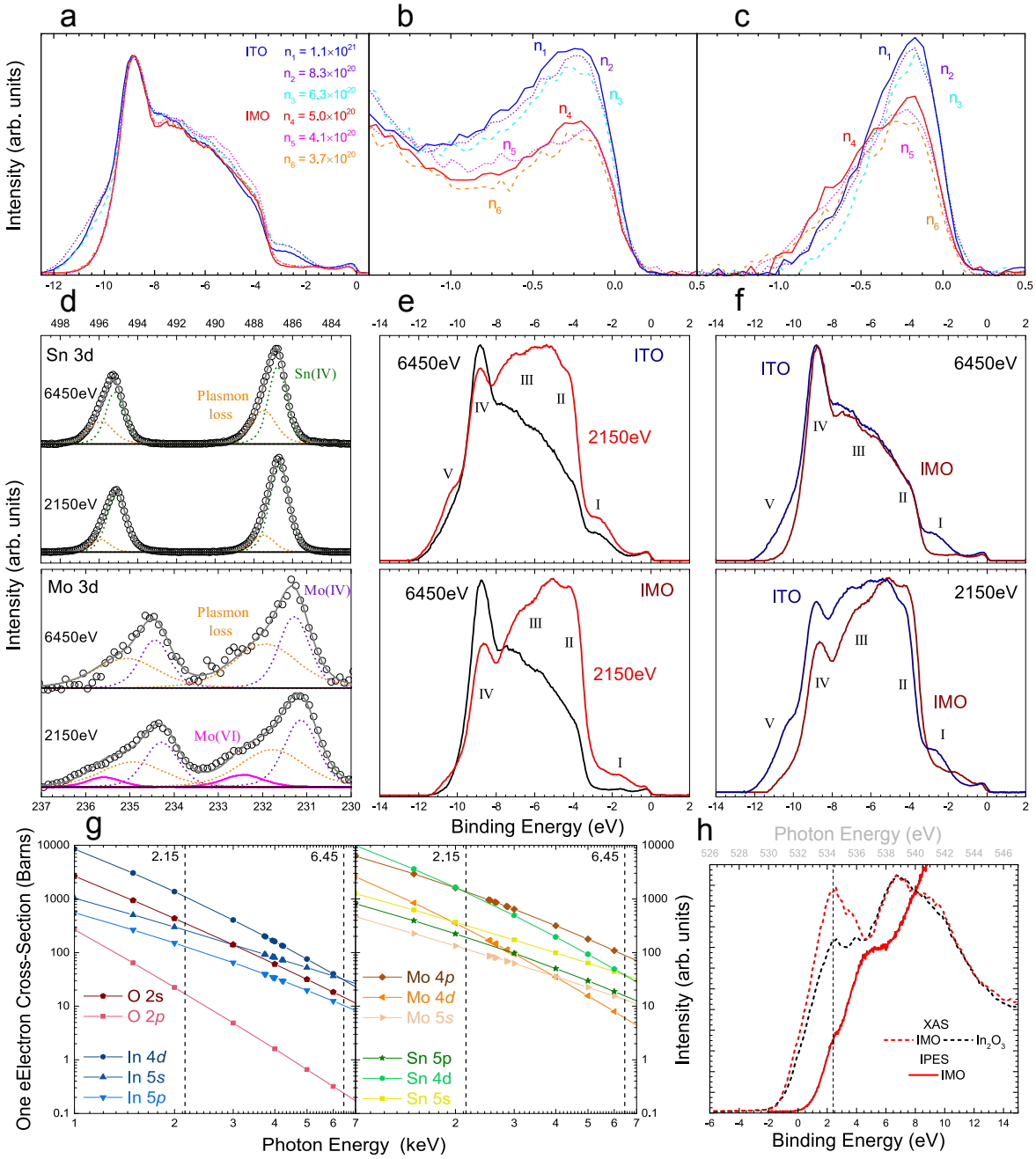


Fig. S5: **a** HAXPES VB spectra for several ITO and IMO films. **b** Conduction band spectra for IMO and ITO. **c** Background subtracted conduction band spectra. Spectra are normalised to the In 5$s$ feature at -9 eV. **d** HAXPES spectra of the Sn 3$d$ and Mo 3$d$ core levels in ITO ($n = 6.3 \times 10^{20}$ cm$^{-3}$) and IMO ($n = 5.0 \times 10^{20}$ cm$^{-3}$) respectively recorded using photon energies of 6450 eV (top) and 2150 eV (bottom). **e** HAXPES VB spectra of the same IMO and ITO films as in **d**. ITO (top) and IMO (bottom) VB spectra at 6450 eV and 2150 eV. **f** Comparison of the VB spectra at 6450 eV (top) and 2150 eV (bottom) for the ITO and IMO films. **g** Photon energy dependence of the one electron photoionization cross-sections for valence orbitals of $In_2O_3$ (left) and Sn and Mo dopants (right). **h** O K-edge XAS of IMO and $In_2O_3$ and IPES spectra of IMO on a common energy scale. The resonant Mo 4$d$ state is seen in both spectra at $\sim 2.3$ eV above the Fermi level.

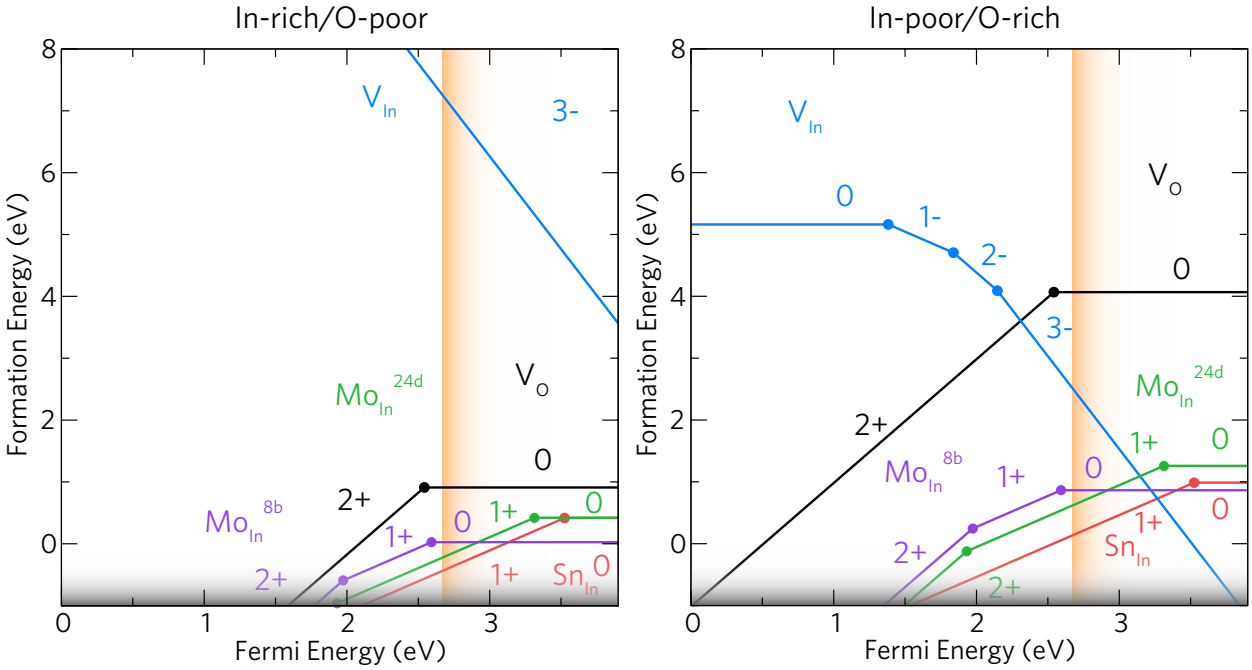


Fig. S6: The thermodynamic transition levels for $In_2O_3$ under *In-rich/O-poor* and *In-poor/O-rich* conditions. The Fermi level ranges from the VBM (0 eV) to the CBM (2.63 eV). The substitutional Mo ($Mo_{In}$) defects are split into the 24d site (green) and the 8b site (purple) in the high-spin configuration (HS) which was found to be the lowest energy configuration for both sites.

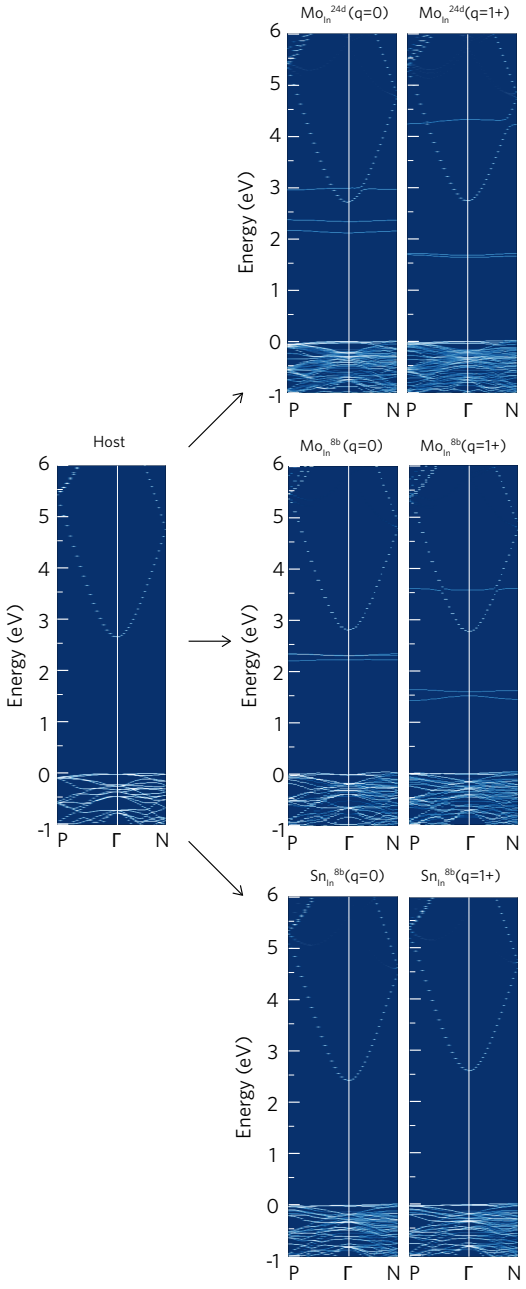


Fig. S7: The unfolded band structure comparison for the undoped host, $Mo_{In}^{24d}$, $Mo_{In}^{8b}$, $Sn_{In}^{8b}$ defects. Each dopant state is represented in the neutral (q=0) and ionised (q=1+) charge state and is represented by the spin-up ($\alpha$) component. The spectral weight of each state is presented by the brightness of the curve.

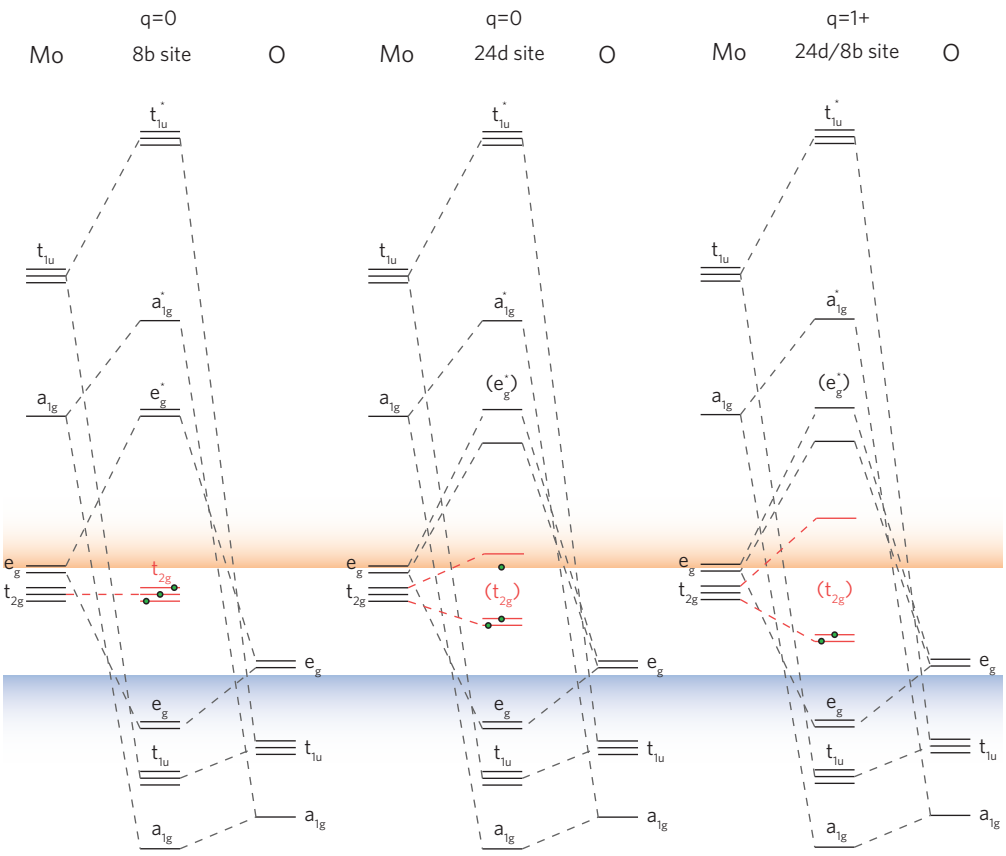


Fig. S8: The schematic molecular orbital diagrams for the $MoO_6$ octahedra on the 8b site, the 24d site in both the q=0 and 1+ charge states. This diagram depicts the Jahn Teller-like distortion that occurs within the $In_2O_3$ lattice, giving rise to the splitting of the degenerate non-bonding $t_{2g}$ state on the Mo. The valence band and conduction bands are represented by the blue and orange regions respectively. Only the electrons corresponding to the $t_{2g}$ site are shown, depicted by the small green circles.

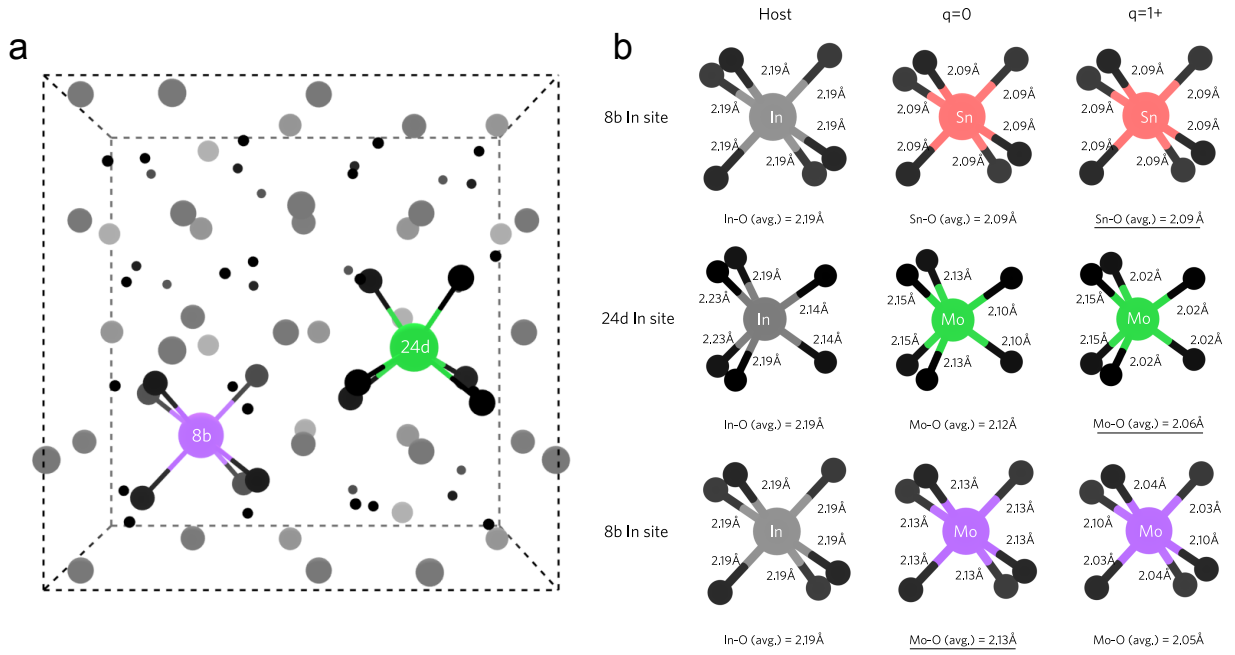


Fig. S9: **a** The two different Wyckoff indium sites within the $In_2O_3$ supercell. The 8b and 24d sites are depicted in purple and green respectively, whilst the oxygens and indium atoms are shown by the black and grey spheres. The 'bonds' are only shown on the highlighted sites for clarity. **b** The M–O octahedra (where M=In, Mo, Sn) for the different In-Wyckoff positions (24d and 8b) and different charge states (q=0 and 1+) showing the different calculated bond lengths. Each dopant site is colour coordinated to the thermodynamic transition levels in Extend Data Fig. S6 whilst the black spheres correspond to oxygen. The expected configuration based on the defect thermodynamics (for Mo and Sn) is shown underlined.

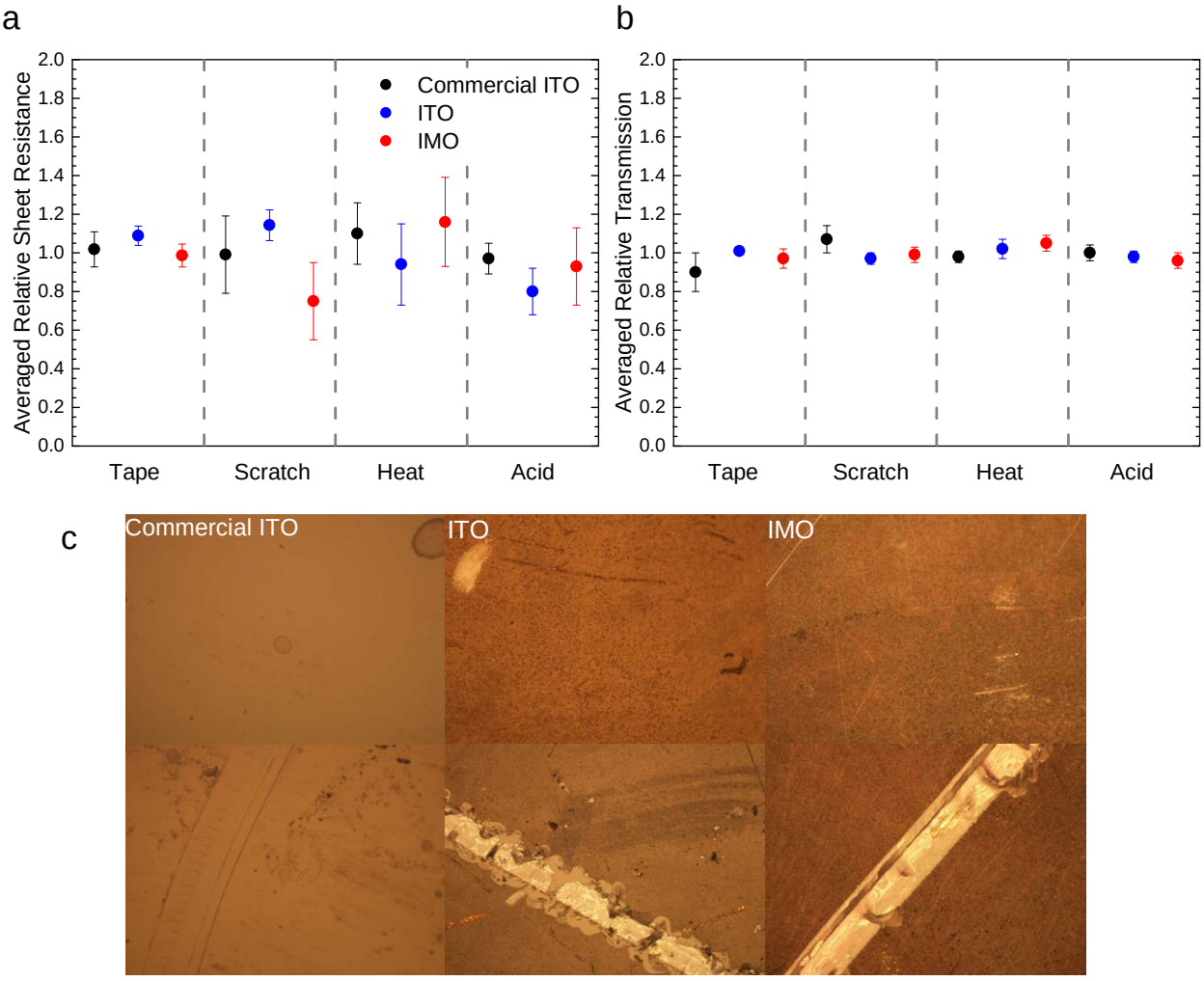


Fig. S10: Durability testing: a) Relative change in sheet resistance between pre and post-test samples. b) Relative change in optical transmission between pre- and post-test samples. c) Optical micrograph of pre-test (top) and post-scratched (bottom) samples.

## 1 Supplementary Results and Discussion

**XRD** X-ray diffraction (XRD) was used to examine the crystal structure and phase of IMO and ITO thin films. Measurements were performed using a Rigaku SmartLab instrument, and patterns collected over $20° < 2\theta < 65°$ with a step size of 0.02°. The patterns shown in Supplementary Fig. S1a confirm the presence of $In_2O_3$ of the cubic bixbyite cubic phase. The films grew with a (400) preferred orientation. The shown calculated pattern was taken from previous refinements[18,19].

**SEM** Scanning electron microscopy (SEM) was used to probe the film morphology. It was also used to estimate the film thickness of each of the IMO and ITO films, which were corroborated by values determined by modelling IR reflectivity data. Cross-sectional images were taken from unmasked samples using a JEOL JSM-6301F Field Emission SEM at an accelerating voltage of 5 keV. A typical cross-section for an IMO and an ITO film can be seen in Supplementary Fig. S1b.

**SIMS** Time of flight secondary ion mass spectrometry (ToF-SIMS) was used to determine the dopant concentration as a function of depth. The Mo and Sn concentrations versus depth beneath the SIMS surface transient region are shown in Supplementary Fig. S2. The SIMS data was calibrated using ion implanted standards. Mo is relatively difficult to detect at dopant concentrations in SIMS with negligible signal being detected from our IMO films for $Mo^+$ and $CsMo^+$ ions. However a clear, but relative noisy signals were obtained for $CsMoO^+$ ions as shown in Supplementary Fig. S2. The equivalent $CsSnO^+$ signal was used to determine the Sn content. The dopant concen-

trations averaged over the depth of each film are compared with the Hall effect electron concentrations in the inset of the figure. To within the measurement uncertainty, the dopant concentrations are equal to electron concentrations. This contrasts with the best performing fluorine-doped tin dioxide transparent conducting films, where there are three dopant atoms per free electron, resulting in significant mobility-limiting compensation.[20] Previously published Sn concentrations versus electron densities for ITO films are also shown for comparison.[1] While many of the data points fall close to the dashed line corresponding to equal dopant and electron concentration, many of the ITO data points at high dopant concentration lie to the right of the line, indicating significantly higher dopant concentration than electron density. Therefore, while compensation can be present in ITO films particularly at very high dopant densities (over $10^{21}$ $cm^{-3}$), our SIMS and Hall effect results indicate that significant compensation due to excess density of dopant atoms is not present in our films. This indicates that IMO films have much better properties than even the best ITO films with negligible compensation.

**Optical characterisation** The free carrier plasma energy and optical gap were determined via reflection and transmission measurements respectively, as seen in Supplementary Fig. S3. Infrared (IR) reflectance measurements were performed using a Bruker Vertex 70v Fourier transform infrared spectrometer at 45° specular reflection. All FTIR measurements were performed with a near-IR light source, $CaF_2$ beam splitter and DLaTGS detector. Due to the nature of specular reflection by non-flat as-grown films, there is a dip in the intensity of the reflection spectra. This phenomena has been observed previously and does not shift the plasma edge [21,22]. Therefore, the plasma energy can be determined by modelling the spectra as described. Transmission measure-

ments were obtained with using a Shimadzu UV-Vis-IR 3700 dual beam spectrophotometer with an integrating sphere and three detectors (photomultiplier, InGaAs and PbS) to cover the whole wavelength range used.

The plasma energies and thicknesses of the films were extracted from IR reflectivity measurements utilizing a two-oscillator dielectric model[23] and transfer matrix method for optical simulation[24]. A four layer (vacuum/$In_2O_3$/$SiO_2$/soda-lime glass) stratified medium was used in the model, with complete incoherence being assumed in the glass substrate and partial incoherence in the vacuum/$In_2O_3$ interface. The absorption spectra were calculated from the transmission spectra of the samples using the Beer-Lambert relation. Optical gaps were extracted from the absorption spectra using a method proposed by Hamberg[2], illustrated by Dolgonos et al[3] which better accounts for the Fermi level being within the conduction band in heavily doped materials compared with the more commonly used Tauc-plot approach.

**Figure of Merit calculations** The performance of a TCO is evaluated in terms of the trade off between the optical transparency and electrical conductivity. The electrical performance of transparent conducting films is often reported as sheet resistance ($R_S$) due to the ease of four point probe measurements, and the invariability of $R_S$ under film size. Often a useful metric to consider is the figure of merit for transparent conductors. The most commonly used definition of the figure of merit is that of Haacke[25]

$$\Phi_H = \frac{T^{10}}{R_S} \tag{1}$$

where transparency, $T$, is taken at $\lambda = 550nm$, the middle of the visible wavelength range and $R_S$ is the sheet resistance. The figure of merit, along with other parameters, is shown for each film in Supplementary Table 1.

Most of the IMO films display signifcantly higher figures of merit compared with those of ITO films. Even for films of similar thickness the $\Phi_H$ value is nearly one-and-a-half times higher for IMO, showing its superior electronic and optical performance.

**Optical gap variation, transport and modelling** Optical gaps determined via transmission measurements (see Supplementary Fig. S3a) versus carrier density from Hall effect measurements are shown in Supplementary Fig. S4a. Equations 3 and 4 were used to model this data, including the effects of variations in band edge effective mass for ITO.

In order to model the optical gap versus the plasma frequency, a carrier statistics model was implemented connecting the two parameters. The plasma frequency is given by

$$\omega_p^2 = \frac{ne^2}{\epsilon_0 \epsilon_\infty \langle m^*(E) \rangle} \tag{2}$$

where $n$ is the free electron concentration, $e$ is the electronic charge, $\epsilon_\infty$ is the high frequency dielectric constant and $\langle m^*(E) \rangle$ is the density of states averaged effective mass accounting for oscillations of free electrons in the conduction band, below the Fermi level $E_F$,

$$\langle m^*(E) \rangle = \frac{\int_0^\infty g(E) m^*(E) f(E, E_F) dE}{\int_0^\infty g(E) f(E, E_F) dE} \tag{3}$$

where the denominator is equal to the free electron density, $n$, and $f(E, E_F)$ is the Fermi-Dirac function and $g(E)$ is the non-parabolic density of states derived from the non-parabolic dispersion relation

$$E\left(1 + \frac{E}{E_g}\right) = \frac{\hbar^2 k^2}{2m^*} \tag{4}$$

where $E_g$ is the fundamental band gap. The optical gap of a degenerately doped semiconductor is usually determined by the lowest energy direct transitions between the valence band maximum (VBM) and the Fermi level in order to account for the conduction band filling. This is complicated for $In_2O_3$ by the transitions from the highest lying valence band states being dipole forbidden[26]. So to model the observed optical transitions, we included an additional 0.8 eV energy separation between the VBM and the highest valence bands for which transitions are dipole allowed.

Supplementary Fig. S4b shows the calculated band edge and DOS-averaged effective masses for IMO and ITO using equation 3. Under Mo doping there is negligible hybridisation between the CBM and and Mo $4d$ dopant states and this means that the band edge effective mass is constant over the whole carrier concentration range. In contrast, as Sn dopants are incorporated into $In_2O_3$, the hybridisation between Sn $5s$ states and the host conduction band around the CBM increases. For ITO as doping increases we see a sharp change in the band edge effective mass, consistent with calculations by Walsh *et al.*[27] Here we arbitrarily assign a carrier density for the onset of hybridisation of $n = 2 \times 10^{20}$ cm$^{-3}$ as we have no Sn doped samples below this carrier density.

Above the Mott criterion ($n \sim 2 \times 10^{18}$ cm$^{-3}$) we see the DOS averaged mass increase for both IMO and ITO. Again they diverge at $n = 2 \times 10^{20}$ cm$^{-3}$ from which the band edge effective

mass of ITO is rapidly increased in order to model the data in Main Fig. 2b.

Free carrier mobilities as a function of carrier concentration are plotted in Supplementary Fig. S4c. Theoretical scattering limits are calculated using the degenerate Brooks-Herring model, modified by Zawadzki[16,28,29] to account for conduction band non-parabolicity, and simplified by Pisarkiewicz *et al.*[17]. We apply the band edge effective mass variation (Supplementary Fig. S4c) determined for ITO. From this we calculate the non-parabolic Fermi level effective mass[30] (as it is the carriers at the Fermi level that are important in scattering events). The theoretical curves reproduce well the divergence of ITO and IMO mobility data at high carrier densities.

**HAXPES spectra and photoionization cross sections** Supplementary Fig. S5 shows hard x-ray photoemission spectra for a range of different dopant concentrations in ITO and IMO films. These spectra can be used to investigate the dependence of the conduction band density-of-states on the carrier concentration. The spectra are normalised to the In $5s$-dominated peak at a binding energy of -9 eV. Immediately we see that samples with higher carrier concentration have a greater intensity just below the Fermi level (zero of the binding energy scale). The spectra from ITO films have more intense peaks than those from IMO, even for films of similar carrier density. By subtracting the background from the conduction band states (due to the Mo $4d$ states in IMO and Sn-Sn disorder-related states in ITO), we can also directly compare the energy widths of the density of states, showing that IMO has lower band edge effective mass, giving lower density of states per energy interval and so greater Burstein-Moss shift than for similar carrier density ITO (see Main Figs 4g and 4h).

High energy x-ray photoemission spectra of the Sn $3d$ and Mo $3d$ core levels are displayed in Supplementary Fig. S5d. Both plots display data taken using photon energies of 6450 eV and 2150 eV, enabling discrimination between bulk and surface features. Spectra have had a Shirley background subtracted and are fitted with Voigt functions. All doublet peak areas have been constrained to a 3:2 ratio consistent with $d$-orbitals, and doublet separations have been constrained (8.4 eV for Sn $3d$ and 3.15 eV for Mo $3d$). The full-width at half maximum of $3d_{5/2}$ and $3d_{3/2}$ peaks from the same chemical species or plasmon loss feature have been constrained to be the same. The binding energy scale is referenced to the Fermi level.

Sn $3d_{5/2}$ and $3d_{3/2}$ core-level peaks were fitted with two components each. The component at 486.7 eV is due to Sn in the Sn(IV) oxidation state, consistent with other measurements[31]. There is no lower binding energy peak and so there is no Sn present in the Sn(II) oxidation state. Hence, the HAXPES data are consistent with Sn acting as a one electron donor in ITO. The component at 487.5 eV is a plasmon loss feature which arises from energy loss of photoelectrons to the free electron gas in conductive materials.[32,33] The positions of the plasmon loss features are constrained to the plasma frequency, $\omega_p$, determined for each film by infrared reflectivity. The plasmon loss component has larger relative intensity when 6450 eV photons are used. This is due to the increased effective probing depth compared with 2150 eV photons and greater probability of energy loss to plasmon excitations for photoelectrons with higher mean free path.

Mo $3d_{5/2}$ and $3d_{3/2}$ core-level spectra are also displayed in Fig. S5d. The lower 2150 eV photon energy data was fitted with three peaks. The first is at 231.2 eV, corresponding to Mo

in the Mo(IV) oxidation state. The second is a plasmon loss peak associated with the Mo(IV) component, lying at higher binding energy by the plasma frequency, $\omega_p \approx 0.6$ eV, measured by infrared reflectivity. The third component is at 232.5 eV. The substitutional Mo has a binding energy very close to that of $MoO_2$ of 231.0 eV,[34] confirming the Mo(IV) oxidation state of the Mo dopant in IMO. We attribute the highest energy component to Mo in the Mo(VI) oxidation state of $MoO_3$ at the surface.[34] This peak is much smaller than the Mo(IV) and is negligibly small in the high photon energy data energy, confirming the surface oxide assignment. This interpretation is consistent with that presented previously for Mo $3d$ data from IMO, but with the improved signal-to-noise ratio and resolution here enabling the identification of the plasmon loss feature associated with the Mo(IV) component. Photoelectrons from the surface $MoO_3$ exit the sample without passing through the IMO and so do not lose energy to the free carrier plasma and so have no associated plasmon loss feature.

Supplementary Fig. S5g shows the one electron photoionization cross-sections calculated by Scofield[35] for the valence electrons states of $In_2O_3$ (O $2s$, O $2p$, In $4d$, In $5s$, In $5p$) and for molybdenum (Mo $4p$, Mo $4d$, Mo $5s$) and tin (Sn $5p$, Sn $4d$, Sn $5s$). When photon energy is increased, all atomic subshell cross sections decrease. However, the O $2p$ subshell experiences a much sharper decline in cross-section. Hence, at higher photon energies, the indium peaks will make a greater relative contribution to the valence band spectra than at lower photon energies. Metal $s$-level cross-sections decline more slowly than the $p$ and $d$ levels as energy increases, resulting in the $s$ levels making a greater contribution to the valence band spectra at higher photon energies.

Supplementary Figs S5e and f show valence band photoemission spectra of ITO and IMO films taken at 6450 eV and 2150 eV. Supplementary Fig. S5e compares the energy dependence of the individual films while Supplementary Fig. S5f compares ITO to IMO at 6450 eV and 2150 eV respectively. All spectra are background subtracted and the spectra are normalised to the maximum intensity. Focusing on Supplementary Fig. S5e, five features are distinguishable in the ITO spectra (labelled I, II, III, IV and V), whilst only four can be seen in the IMO (I, II, III, IV). Using our DFT calculated electronic partial density of states we can distinguish these features. I represents the sub-gap feature in each case. The IMO sub-gap feature is due to two occupied Mo $4d$ bands while the ITO feature is associated with some level of Sn-Sn disorder in the films.[36] Feature II is due to O $2p$-In $4d$ dominated VBM, while III is due to mainly to O $2p$-In $5p$ mixing. Feature IV is the bottom of the VBM, comprising mainly O $2p$ and In $5s$ states. Finally, feature V that is only present in ITO is due to Sn $5s$ states.

Feature IV is the dominant peak at 6450 eV when the In $5s$ states dominate and the O $2p$ intensity is reduced by its low relative cross section giving a weak feature II. At 2150 eV, the dominant peak is feature III which is primarily O $2p$ and In $5p$. Laboratory Al K$\alpha$ x-ray sources of energy 1486.6 eV display feature II as the strongest peak, when the O $2p$ states dominate due to their higher relative higher cross section at low photon energy.[32] Measurements over a range of photon energies clearly show the effect on the valence band spectra of the rapidly changing O $2p$ cross section.

The right-hand panel shows a comparison of IMO to ITO at 6450 eV (top) and 2150 eV

(bottom). At high photon energy, the data from the two materials is very similar except for features I and V which originate from the dopant related states. At low photon energy, the differences across the valence band spectra are more pronounced. This is due to the different hybridization of Sn and Mo with the O states which make a greater contribution to the valence band spectra at low photon energy when they have higher relative cross sections. Some level of conduction band emission can be seen in all spectra and is associated with the degenerate doping of these films.

**X-ray absorption spectra of IMO and undoped $In_2O_3$ and IPES of IMO** X-ray absorption spectroscopy (XAS) can be used to probe the unoccupied states of a material above the Fermi level. We employ this technique here in this study to provide support for the assignment of the Mo $4d$ states in our IPES spectra. O K-edge absorption spectra of IMO and nominally undoped $In_2O_3$ were recorded in partial electron yield mode. The photon energy was calibrated using a $TiO_2$ reference, which was then aligned with the Fermi level using the O $1s$ peak from our HAXPES measurements with a 1 eV core hole correction.[37] This is plotted in Supplementary Fig. S5h along with our IPES spectra for IMO and undoped $In_2O_3$ films. The oxygen partial density of states in the XAS plot has a much higher intensity at around $\sim 2.3$ eV, in excellent agreement with the Mo $4d$ feature seen in the IPES. This is indicative of some hybridization of the Mo $4d$ states with the oxygen states. The alignment of these features after independent charge referencing supports the identification of the unoccupied Mo $4d$ state as the donor in IMO films.

## Computational Methodology

Hybrid density functional theory (DFT) calculations were carried out on $In_2O_3$ using a plane-wave

basis within the periodic code, VASP.[38–41] The projector augmented wave method (PAW)[42] was used to describe the interaction between the core electrons (In[Kr], O[He], Sn[Kr], Mo[Kr]) and valence electrons. In order to relax the structural and electronic properties of bulk $In_2O_3$ the HSE06 (Heyd-Scuseria-Ernzerhoff)[43,44] hybrid functional was used. HSE06 incorporating 25% of exact Fock exchange to the PBE formalism with a screening parameter ($\omega = 0.20\,\text{bohr}^{-1}$) has been shown to accurately describe the structural and electronic properties of $In_2O_3$ and its polymorphs.[32,45–51] The primitive cell of bixbiyite $In_2O_3$ (space group $Ia\bar{3}$, 40 atoms) was subjected to a geometry optimisation using a 450 eV plane wave cutoff and a $\Gamma$-centred $k$-point grid of $4\times4\times4$ for adequate convergence which was deemed to be complete when the residual forces on all atoms was less than 0.01 eV $\text{Å}^{-1}$. In order to calculate the defect thermodynamics, the conventional cell of $In_2O_3$ (80 atoms) was relaxed using a 450 eV plane wave energy cutoff and a $\Gamma$-centred $2\times2\times2$ $k$-point grid with only the ions within the cell permitted to move to a force convergence of 0.01 eV $\text{Å}^{-1}$.

The dopant-related limiting phases were also relaxed using the same relaxation conditions as the primitive cell and are tabulated in Supplementary Table S2 showing the space groups, $k$-point meshes and enthalpies of formation ($\Delta H_f$) in relation to experimental room-temperature values. The calculated 0 K values are in reasonable agreement with the experimental values.[52] The difference can be accounted for by temperature and entropic effects, as well as choice of hybrid functional.[33,53]

Table S2: The tabulated limiting phases belonging to the dopant species as calculated with the PBE0 hybrid functional. Included is the space group, the Γ-centred $k$-point meshes used for convergence as well as the enthalpy of formation (experimental room temperature values[52] in parentheses).

| Limit | Spacegroup | $k$-point mesh | $\Delta H_f$ /eV |
|---|---|---|---|
| $SnO_2$ | $P4_2/mnm$ | $8 \times 5 \times 5$ | -5.31 (-5.99) |
| $MoO_2$ | $P2_1/c$ | $5 \times 4 \times 5$ | -5.38 (-6.09) |
| $MoO_3$ | $Pbnm$ | $6 \times 2 \times 6$ | -6.52 (-7.72) |

**Defect Formalism** For a defect in charge state $q$, the enthalpy of formation at the *athermal* limit can be described as:

$$\Delta H_f(D,q) = (E^{D,q} - E^{H}) + \sum_i n_i(E_i + \mu_i) + q(E_{\text{Fermi}} + \epsilon^{H}_{VBM} + \Delta\,\nu^{\text{pot}}) + E_{\text{corr}} \qquad (5)$$

where $E^{\text{H}}$ and $E^{D,q}$ are the total energies of the host and defective supercells respectively. The enthalpy of formation is then related to the sum of the chemical potentials, $\mu_i$ and the elemental energy $E_i$ ($In_s$, $O_{2(g)}$, $Sn_{(s)}$, $Mo_s$). $n_i$ refers to the number of electrons added or taken away from an external reservoir.[54] The Fermi level, $E_{\text{Fermi}}$ ranges from the VBM (0 eV) to the CBM (2.63 eV) and $\epsilon^{H}_{VBM}$ refers to the VBM eigenvalue of the host supercell. The potentials of the defective supercell and the host supercell are aligned using the correction term, $\Delta\,\nu^{\text{pot}}$, which averages the potential of the supercell bar the immediate vicinity of the defect.[55]

In order to regain the 'dilute-limit', post-processing corrections ($E_{\text{corr}}$ are applied due to the finite-size effects present in supercells. Firstly an *image-charge* correction is applied which

minimises the long-ranged nature of the Coulomb interaction[56,57] of the charged defect and its periodic images. The scheme implemented herein uses a formalism based on the Lany and Zunger correction[55] by Hine and Murphy.[57,58] A band filling correction is also applied to shallow and resonant defects to account for the high carrier concentrations present in supercell calculations in a formalism by Lany and Zunger.[55,59]

**Thermodynamic Limits** The equilibrium growth conditions of $In_2O_3$ can be reflected by the chemical potentials ($\mu_i$) which can be varied to simulate the experimental partial pressures. $mu_{\mathrm{In}}$ and $\mu_{\mathrm{O}}$ can then be evaluated via the calculated formation enthalpy of the host:

$$2\mu_{\mathrm{In}} + 3\mu_{\mathrm{O}} = \Delta H_f^{\mathrm{In_2O_3}} = -9.47\,\mathrm{eV} \tag{6}$$

The experimentally determined standard enthalpy of formation for $In_2O_3$ is -9.57 eV[60] in close agreement with our calculated value at 0 K.

This formation enthalpy allows for the calculation of a range of growth conditions bounded by two growth conditions which are:

*In-rich/O-poor* bound limited by the formation of metallic In ($In_{(s)}$):

$$\Delta\mu_{\mathrm{In}} = 0; \Delta\mu_{\mathrm{O}} = -3.16\,\mathrm{eV} \tag{7}$$

and an *In-poor/O-rich* bound limited by the formation of oxygen gas, $O_{2(g)}$

$$\Delta\mu_{\mathrm{O}} = 0; \Delta\mu_{\mathrm{In}} = -4.73\,\mathrm{eV} \tag{8}$$

The solubility of Sn and Mo within the bixbyite lattice is limited by the formation of dopant phases; $SnO_2$, $MoO_2$ and $MoO_3$ or elemental Sn and Mo.

Under *In-rich/O-poor* conditions, $\mu_{\mathrm{Sn}}$ and $\mu_{\mathrm{Mo}}$ are limited via the formation of $\mathrm{Sn_s}$ and $\mathrm{Mo_s}$ respectively giving values of 0 eV for each respectively. Under a *In-poor/O-rich* regime, $\mu_{\mathrm{Sn}}$ and $\mu_{\mathrm{Mo}}$ are now limited via the formation of $SnO_2$ and $MoO_3$ conditions respectively. The chemical potentials are therefore $\Delta\mu_{\mathrm{Sn}}$=-5.31 eV and $\Delta\mu_{\mathrm{Mo}}$=-6.52 eV respectively.

The thermodynamic transition levels can be calculated for a given defect at a specific Fermi level for the transition from $q$ to $q'$ by:

$$\epsilon_D \frac{q}{q'} = \frac{\Delta H_f(D,q) - \Delta H_f(D,q')}{q' - q} \tag{9}$$

**Band-Structures** Due to the shrinking of the Brillouin zone, supercell calculations result in folded band structures. In order to regain a representation of the *primitive* or *conventional* cell, the band unfolding code, *BandUp* was used. Band unfolding is a methodology described by Popescu and Zunger[61] and is implemented in a python package by Medeiros and Björk.[62,63] The unfolded band structures are shown in Supplementary Fig. S7.

**Calculated Undoped Bulk Structural and Electronic Properties** The structural and electronic properties of $In_2O_3$ were calculated using the HSE06 hybrid functional. Indium sesquioxide crystallises within the bixbyite ($Ia\bar{3}$) crystal structure which results in an array of distorted $InO_6$ octahedra. There are two different In environments (Wyckoff positions: 8b and 24d as shown in Supplementary Fig. S9) within the $In_2O_3$ lattice and one oxygen site (48e). The relaxed cell lengths, angles, In–O bond lengths, fundamental band gap ($\mathrm{E_g^{fund}}$) and effective masses of the valence ($\mathrm{m^*_{VBM}}$) and conduction ($\mathrm{m^*_{CBM}}$) bands are given in Supplementary Table S3, alongside

previous HSE06 and experimental values.

The structural parameters calculated in this study are in very close agreement with experimental values and in reasonable agreement with previous HSE06 calculated parameters (the difference likely arising due to varying energy cuttoffs and $k$-point meshes) showing the efficacy of HSE06 in reproducing the structural properties of $In_2O_3$.[45,46,49,64–71]

The $In_2O_3$ band structure is given in Main Fig. 3a. The valence band maximum (VBM) is made up of predominantly O $2p$ states ($\sim$90%) mixed with some In $4d$ ($\sim$10%) states. The conduction band minimum on the other hand is made up of predominantly unoccupied In $5s$ states ($\sim$67%) with some O $2p$ mixing ($\sim$33%). The separation between VBM and CBM at $\Gamma$ gives a direct fundamental band gap of 2.63 eV (the indirect band gap is around 0.001 eV lower in magnitude) which matches the weak absorption onset seen in $In_2O_3$ experiment.[72] Previous theory and x-ray spectroscopy has shown that the optical gap arises from an allowed transition from $\sim$0.8 eV below the VBM giving rise to the well recorded strong absorption onset at $\sim$3.5-3.7 eV for undoped $In_2O_3$.[2,21,26,72] The hole effective masses at the VBM are extremely high, over $14m_e$, indicative of the highly localised O $2p$ nature. The average CBM electron effective mass is $0.22m_e$ which matches previous HSE03 calculations[69] and is within the range of experimental values of 0.18-0.22$m_e$ [68,73] and gives rise to high mobility in doped $In_2O_3$.

Table S3: The bulk $In_2O_3$ structural and electronic parameters as calculated with the HSE06 hybrid functional compared to previous HSE06 (except where stated) calculations and experiment.

| Parameters | This work | HSE06 (lit.) | Experiment |
|---|---|---|---|
| $a = b = c$ (Å) | 10.15 | 10.23[45,64] | 10.12[65] |
| $\alpha = \beta = \gamma$ (°) | 90 | 90[45] | 90[65] |
| In-O (Å) | 2.14, 2.20, 2.23 | 2.15[49] | 2.13, 2.19, 2.23[65] |
| $E_g^{fund}$ (eV) | 2.63 eV | 2.20[45], 2.6[64], 2.74[46] | 2.62[66], 2.63[67] |
| $m^*_{VBM}$ ($m_e$) | 14.70 | 16.14 (PBE)[27] | - |
| $m^*_{CBM}$ ($m_e$) | 0.22 | 0.22 (HSE03)[69] | 0.18-0.22[68,70,71,73] |

**Dopant and Defect Thermodynamics and Structural Analysis** Mo and Sn substitutional doping was simulated alongside the dominant donor and acceptor native defects in $In_2O_3$ using the HSE06 functional. Supplementary Fig. S6 displays the thermodynamic transition levels under *In-rich/O-poor* and *In-poor/O-rich* conditions respectively.

**Intrinsic Defects** Under both *In-rich/O-poor* and *In-poor/O-rich* conditions respectively, $V_{\mathrm{In}}$ is a high formation energy *ultra-deep* acceptor defect. Out of the two In sites in $In_2O_3$ the lowest formation energy site (for $V_{\mathrm{In}}$) is found to be the 24d Wyckoff position (by $\sim$0.19 eV) which has also been found in previous hybrid calculations.[49] The neutral charge state has a formation energy of 9.89 eV and 5.16 eV under *In-rich/O-poor* and *In-poor/O-rich* conditions respectively. The 0/1- charge state occurs around 1.38 eV above the VBM followed by further transition levels: 1-/2- and -2/-3 at 1.84 eV and 2.15 eV above the VBM respectively. $V_{\mathrm{In}}$ is therefore not a cause of any $p$-type conductivity. For $V_{\mathrm{In}}^0$, the three induced holes are localised on neighbouring oxygen $2p$ orbitals. Correct localisation of electrons and holes is critical for the accurate description of the total energies and thus the formation energies of defects in materials and has been shown for $V_{\mathrm{Zn}}$ in ZnO.[53,74] Previous HSE06 calculations on $V_{\mathrm{In}}$ corroborate these results.[49,64,75]

$V_{\mathrm{O}}$ is a negative-U deep donor defect under both growth regimes with a 2+/0 transition level occuring around 0.13 eV below the CBM. This behaviour is similar to other binary $n$-type TCOs such as $SnO_2$[76], ZnO[53] and $BaSnO_3$[77]. Under $n$-type favourable *In-rich/O-poor* conditions $V_{\mathrm{O}}^0$ has a formation energy of 0.91 eV which rises to 4.07 eV under *In-poor/O-rich* conditions. These results suggest that $V_{\mathrm{O}}$ will be both prevalent and a minor source of $n$-type conductivity in $In_2O_3$.

In the neutral charge state ($V_O^0$), the electron density is highly localised as seen in previous theory results on $V_O$ in $In_2O_3$.[75] Intrinsic compensation by $V_{In}^{3-}$ occurs $\sim$2.1 eV above the CBM under *In-rich/O-poor* conditions and around 0.41 eV *below* the CBM under *In-poor/O-rich* conditions.

**$Sn_{In}$ and $Mo_{In}$** $Sn_{In}$ acts as a low formation energy *resonant* donor under both *In-rich/O-poor* and *In-poor/O-rich* conditions with formation energies for the neutral charge state of 0.42 eV and 0.99 eV respectively. Sn preferentially sits on the 8b Wyckoff site in correlation with previous theory results.[32,49] The 1+/0 transition level occurs around 0.85 eV above the CBM which allows for very high carrier concentrations as seen in experiment, and through Moss-Burstein shifts of $\sim$0.85 eV.[32] Under *In-poor/O-rich* conditions, $Sn_{In}$ is compensated for by $V_{In}^{3-}$ around 0.55 eV above the CBM trapping the Fermi level just below this point.

Due to Mo possessing three additional valence electrons to In, two spin states were modelled: a *high-spin* (denoted 'HS' and involves three electrons in the spin-up ($\alpha$) component) and a *low-spin* (denoted 'LS' and involves two electrons in the spin-up and one in the spin-down ($\beta$) component). The two inequivalent In sites (corresponding to 24d and 8b Wyckoff positions) were also assessed in this study for each spin configuration.

From the HSE06 relaxations it was shown that the high-spin configurations for the neutral charge state possessed the lowest formation energies for both the 8b and 24d sites by $\sim$0.87 eV and $\sim$0.31 eV respectively. These results are in keeping with a previous study by Xu et al. who predict this as the ground state configuration of substitutional Mo in the $In_2O_3$ lattice. $Mo_{In}^{8b}$ acts as a *deep* defect with a 1+/0 transition level occurring around 0.08 eV below the CBM.[78] The neutral

charge state possesses a formation energy of 0.02 eV and 0.86 eV under *In-rich/O-poor* and *In-poor/O-rich* conditions respectively, making Mo on this site a highly soluble dopant. Two further transition levels occur within the band gap: a 2+/1+ and 3+/2+ transitions around 0.70 eV and 1.59 eV below the CBM respectively. $Mo_{In}^{24d}$ on the other hand acts as a *resonant* one-electron donor with the 1+/0 transition level occurring around 0.64 eV above the CBM. Despite the neutral charge state of $Mo_{In}^{24d}$ possessing a formation energy of 0.42 eV and 1.25 eV under *In-rich/O-poor* and *In-poor/O-rich* conditions respectively, this charge state is only reached at Fermi levels far above the CBM. From Supplementary Fig. S6, the ionised charge state (1+) possesses a lower formation energy at the CBM and thus it can be rationalised that $Mo_{In}^{24d}$ is the *dominant* dopant species to be present in the $In_2O_3$ lattice. As with the 8b site, the 2+/1+ and 3+/2+ transition levels occur deep within the band gap around 0.74 eV and 1.35 eV below the CBM.

Supplementary Fig. S9b displays the calculated bond lengths present in the $In_2O_3$ lattice as a set of $MO_6$ (where M=In, Mo or Sn) octahedra relating to the 8b and 24d In sites. For undoped $In_2O_3$ the average In–O bond lengths (for both 8b and 24d sites) are 2.19 Å which correspond well to EXAFS studies on $In_2O_3$ which quote values in the range of 2.16–2.18 Å [5,79,80] which are within 1.5% of the HSE06 calculated values. The Sn–O bond lengths contract uniformly to around 2.09 Å in both the neutral and 1+ charge state (ionised). These values are in keeping with experimental EXAFS values of $\sim$2.05–2.08 Å for ITO.[79]

In Mo-doped $In_2O_3$ the 24d site shows a contraction of the bond lengths from the neutral (q=0) to the ionised (q=1+) charge states (Supplementary Fig. S9b with an average bond length of

2.12 Å and 2.06 Å respectively. For the 24d site, Mo will be ionised within the $In_2O_3$ lattice, therefore the relaxed q=1+ structure is likely to be seen and matches well with EXAFS measurements of 2.05 Å for Mo–O.[5] Further analysis of the Mo–In bond lengths gives rise to two (average) values of 3.38 Å and 3.84 Å which are in excellent agreement with the EXAFS values of 3.36 Å and 3.82 Å .[5] When incorporated on the 8b In site, the Mo–O bonds contract uniformly compared to the In–O bond lengths, giving rise to an average bond length of 2.13 Å. In the 1+ charge state, $Mo_{In}^{8b}$ undergoes a further contraction of the bond lengths, however *non-uniformly*, with a Jahn-Teller distortion occurring (equatorial Mo–O:2.03–2.04 Å , axial Mo–O:2.10 Å ). Although the average bond lengths correspond to 2.05 Å which matches the EXAFS literature values, as $Mo_{In}^{8b}$ is a thermodynamically *deep* defect. It is expected to exist in the neutral charge state at Fermi levels at and above the CBM.

**Electronic Structure** The unfolded bandstructures relating to the undoped host, $Mo_{In}$ on the 24d and 8b sites (HS) and $Sn_{In}$ were calculated and are shown in Supplementary Fig. S7. Both the neutral (q=0) and ionised (q=1+) charge state for each dopant was calculated to compare the electronic structure arising from the structural changes upon relaxation. In the high-spin configurations, the dopant states occur in the spin-up ($\alpha$) component (in the energy range -1–6 eV) and as such the spin-down ($\beta$) component is not shown in this comparison. From the HSE06 calculations, the density of states at the CBM is found to be around 3% Sn $s$ character. This hybridisation has the effect of raising the electron effective mass by reducing the dispersion. This effect is seen in previous band structure calculations containing corrections to enable a more reliable description of the effective mass changes for $In_2O_3$ with a change in band edge effective mass upon Sn doping from

0.22 $m_e$ to 0.40 $m_e$ (Ref. 27). The Sn 5$s$ atomic orbital level lies directly between the O 2$p$ and In 5$s$ levels, resulting in strong hybridization with the In 5$s$-O 2$p$-dominated CBM. The partial charge density of the CBM in Main Fig. 3 displays the electron density delocalised over the In $s$, O $p$ and Sn $s$ states. This hybridisation explains the perturbation of the CBM dispersion upon Sn-doping which leads to the increased band edge effective mass.

In Mo-doped $In_2O_3$, the two different In Wyckoff sites give rise to different electronic structures. In the neutral charge state, $Mo_{In}^{24d}$ displays negligible Mo hybridisation at the CBM and instead two *filled* bands of Mo 4$d$ character exist in the band gap around 2.11 eV and 2.33 eV above the VBM respectively. A further empty band occurs around 2.98 eV above the VBM ($\sim$0.31 eV above the CBM) also of $\sim$73% Mo 4$d$ character.

In its ionised form (q=1+), Mo(IV) oxidation state, $Mo_{In}^{24d}$ displays an enhanced splitting of the Mo bands with the two filled bands lowering in energy in the band gap to around 1.66 eV and 1.67 eV above the VBM. These are depicted in a partial charge density plot in Main Fig. 3. The Mo 4$d$ band above the CBM is raised to 4.25 eV above the VBM (1.58 eV above the CBM) and is depicted in Main Fig. 3. These results correspond well to the inverse photoemission spectra (Main Fig. 4d), with the unoccupied Mo 4$d$ being observed only about 0.5 eV higher than calculated by DFT. This also highlights the short comings of the findings of Xu *et al.*[78] who do not take into account the ionised dopant state for any of their transition metal-doped TCO calculations. Without considering the ionised dopant state, the calculation of the dopant $d$ energy levels is erroneous and so it is impossible to determine reliably whether a particular dopant will perform well. The fact that

their neutral charge state calculations give a $d$ level close to the CBM explains why they suggest Mo will not produce good electrical properties in $In_2O_3$. This is despite previous experimental evidence to the contrary which is now rationalised by our theoretical results giving the donor $d$ level far above the CBM for the 1+ Mo charge state.

As there is negligible Mo $d$ state contribution at the CBM, Mo does not perturb the CBM dispersion, allowing IMO to retain the host $In_2O_3$ band edge effective mass, resulting in the high electron mobilities seen in this work and previous literature.[5] Main Fig. 3 depicts the CBM for the Mo (24d)-doped $In_2O_3$ cell showing the absence of any electron density contribution from Mo. The cause of the Mo $4d$ splitting can be attributed to the Jahn-Teller-like distortion $Mo_{In}^{24d}$ in the neutral charge state which, in the 1+ charge state increases due to the further contraction of the bond lengths further splitting the levels. This can be rationalised using crystal-field splitting seen in the simplified molecular orbital diagram for $MoO_6$ octahedra in Supplementary Fig. S8.

When doped on the 8b site, $Mo_{In}$ possesses three *filled* Mo $4d$ bands in the band gap at 2.23 eV, 2.31 eV and 2.31 eV respectively. As the 8b In site is only slightly distorted from the perfect octahedral ($O_h$) symmetry, a slight splitting of the degenerate non-bonding $t_{2g}$ levels is expected (see Supplementary Fig. S8). As the Mo–O bond lengths are uniform with little distortion around the $Mo_{In}$ in the neutral charge state (see Supplementary Fig. S8), three occupied non-bonding Mo $4d$ bands are seen in the band gap. Mo can therefore be seen to exist as Mo(III) in this configuration. As with the 24d site, $Mo_{In}^{8b}$ undergoes a further splitting of the $t_{2g}$ bands in its ionised form due to a similar Jahn-Teller distortion. Here, the two $4d$ states in the band gap appear

at 1.51 eV and 1.59 eV above the VBM respectively whilst the third unoccupied band exists around 3.57 eV above the VBM ($\sim$ 0.89 eV above the CBM).

**Durability testing** This research shows that IMO has a fundamentally better optoelectronic properties than ITO. As it is also a cost effective replacement for ITO, from these considerations, it should take its place in the transparent conductors market. However, any replacement for ITO must also be at least as durable - it must withstand the wear and tear and environmental conditions it is likely to be exposed to in typical uses. ITO is predominantly used as an electrode in modern electronic devices, such as touch screens and televisions. Hence, these films are nearly always encapsulated in a device which offers the film a lot of protection. The conditions ITO is exposed to our arguably less harsh than those experienced by FTO in low emissivity window coatings and in solar cells. Nevertheless, we have performed simple lab-based tests in order to simulate some different environmental stresses on our IMO and ITO films, and on a commercially available product (Ossila ITO film on glass substrate, $d = 100nm$, $R_s = 20\Omega/\Box$) for comparison.

All durability tests were repeated several times to enable the uncertainty in the change of sheet resistance and transmission to be given as the standard deviation in the results. Sheet resistance of films was determined using a CMT-SR2000 4-point probe system and transmission was measured using a Shimadzu UV-Vis-IR 3700 spectrophotometer. Sheet resistance values were averaged over a number of measurements across each sample. Transmission values were taken at wavelengths of $\lambda$ =500nm, 700nm, and 1250nm to give a reasonable representation of the whole spectrum. Finally, the relative values of both the sheet resistance and transmission were found by

dividing the measured value post-test by that of a pre-test sample (i.e. a relative sheet resistance ¿1 indicates the test increased the sheet resistance).

Optical Microscopy was performed using a Nikon Eclipse LV100 microscope in bright field setting at $\times 20$ optical zoom. Optical measurements were performed after each test, although little difference was noticeable except subsequent to scratch testing when the obvious imprint of the scratch could be seen.

The scotch tape test was performed using Intertape LA-26 Polyester Laminate Tape. Adhesive tape was pressed onto films and left to set. Subsequent removal of the tape allows a measure of film de-lamination. None of the films showed any signs of de-lamination as indicated in Supplementary Fig. S10a and b.

The scratch test was performed using an Elcometer 3092 sclerometer which has a tungsten carbide tip and a maximum 20N force spring which was utilised for all measurements. Supplementary Fig. S10a shows some changes to the sheet resistance following the scrathc test, with a slight increase for ITO and small decrease for IMO. However, the statistical uncertainty on these measurements was greater than after the tape test, indicating that there is differences are not significant. The optical transmission post scratch test was unchanged, as shown in Figure S10b. The optical micrographs shown in Figure S10c clearly demonstrate the difference is morphology of the three films (top row) and the effect that the tungsten carbide tip has on the films. The commercial ITO is thinner than our films and has a lower degree of surface roughness which is apparent in the micrograph, appearing less opaque and less granular (less light scattering from the surface). The

scratch applied to the commercial ITO does not seem to penetrate deep, likely due to the film being much thinner. Our films seem to be penetrated more deeply with a noticeable difference in depth of field. However, this again does not appear to have greatly effected the electronic or transmissive properties and so is of little concern.

Films were heated in a furnace in ambient at 250°C for three hours to simulate the effects of heat expelled from components in an electronic device. Supplementary Fig. S10a and b again demonstrate all films performed well in the tests in terms of electronic and optical properties.

Finally films were immersed in dilute sulfuric acid for three hours. The acid had a pH of around 3.5, slightly more acidic than acid rain or sweat which are the most likely acids to come into contact with the films in applications. No appreciable sheet resistance or optical losses were noticeable post treatment, as can be seen in Supplementary Fig. S10a and b.

These tests demonstrate that CVD IMO can withstand general wear and tear and environmental conditions as well as both a commercially produced ITO film and ITO deposited using the same technique. This indicates that, subject to more extensive industrial durability testing, there are no barriers to the widespread adoption of IMO as a superior replacement for ITO.

1. Bierwagen, O. & Speck, J. S. Plasma-assisted molecular beam epitaxy of Sn-doped $In_2O_3$: Sn incorporation, structural changes, doping limits, and compensation. *Phys. Stat. Sol. (a)* **211**, 48–53 (2014).

2. Hamberg, I., Granqvist, C. G., Berggren, K. F., Sernelius, B. E. & Engström, L. Band-gap widening in heavily Sn-doped $In_2O_3$. *Physical Review B* **30**, 3240–3249 (1984).

3. Dolgonos, A., Mason, T. O. & Poeppelmeier, K. R. Direct optical band gap measurement in polycrystalline semiconductors: A critical look at the tauc method. *Journal of Solid State Chemistry* **240**, 43–48 (2016).

4. Parthiban, S., Elangovan, E., Ramamurthi, K., Martins, R. & Fortunato, E. Investigations on high visible to near infrared transparent and high mobility Mo doped $In_2O_3$ thin films prepared by spray pyrolysis technique. *Solar Energy Materials and Solar Cells* **94**, 406–412 (2010).

5. Bhachu, D. S. *et al.* Origin of high mobility in molybdenum-doped indium oxide. *Chemistry of Materials* **27**, 2788–2796 (2015).

6. Meng, Y. *et al.* A new transparent conductive thin film $In_2O_3$:Mo. *Thin Solid Films* **394**, 218–223 (2001).

7. Parthiban, S., Ramamurthi, K., Elangovan, E., Martins, R. & Fortunato, E. Spray deposited molybdenum doped indium oxide thin films with high near infrared transparency and carrier mobility. *Applied Physics Letters* **94**, 212101 (2009).

8. Yamada, N. *et al.* High-throughput optimization of near-infrared-transparent Mo-doped $In_2O_3$ thin films with high conductivity by combined use of atmospheric-pressure mist chemical-vapor deposition and sputtering. *Thin Solid Films* **626**, 46–54 (2017).

9. Meng, Y. *et al.* Molybdenum-doped indium oxide transparent conductive thin films. *Journal of Vacuum Science & Technology A* **20**, 288–290 (2002).

10. Tahar, R. B. H., Ban, T., Ohya, Y. & Takahashi, Y. Tin doped indium oxide thin films: Electrical properties. *Journal of Applied Physics* **83**, 2631–2645 (1998).

11. Groth, R. Untersuchungen an halbleitenden indiumoxydschichten. *physica status solidi* **14**, 69–75 (1966).

12. Mizuhashi, M. Electrical properties of vacuum-deposited indium oxide and indium tin oxide films. *Thin Solid Films* **70**, 91–100 (1980).

13. Clanget, R. Ionized impurity scattering in degenerate $In_2O_3$. *Applied Physics* **2**, 247–256 (1973).

14. Song, P. K., Shigesato, Y., Kamei, M. & Yasui, I. Electrical and structural properties of tin-doped indium oxide films deposited by DC sputtering at room temperature. *Japanese Journal of Applied Physics* **38**, 2921–2927 (1999).

15. Shigesato, Y., Takaki, S. & Haranoh, T. Electrical and structural properties of low resistivity tin-doped indium oxide films. *Journal of Applied Physics* **71**, 3356–3364 (1992).

16. Zawadzki, W. Electron transport phenomena in small-gap semiconductors. *Advances in Physics* **23**, 435–522 (1974).

17. Pisarkiewicz, T., Zakrzewska, K. & Leja, E. Scattering of charge carriers in transparent and conducting thin oxide films with a non-parabolic conduction band. *Thin Solid Films* **174**, 217–223 (1989).

18. Marezio, M. Refinement of the crystal structure of $In_2O_3$ at two wavelengths. *Acta Crystallographica* **20**, 723–728 (1966).

19. Zachariasen, W. The crystal structure of the modification $C$ of the sesquioxides of the rare earth metals, and of indium and thallium. *Norsk Geologisk Tidsskrift* **9**, 310–316 (1927).

20. Swallow, J. E. N. *et al.* Self-compensation in transparent conducting F-doped $SnO_2$. *Adv. Funct. Mater.* **28**, 1701900 (2018).

21. Köstlin, H., Jost, R. & Lems, W. Optical and electrical properties of doped $In_2O_3$ films. *Physica Status Solidi (a)* **29**, 87–93 (1975).

22. Dobberstein, P., Hampe, A. & Sauerbrey, G. Absorption of light by surface plasmon excitation. *Physics Letters A* **27**, 256–257 (1968).

23. Pickering, C. Infrared reflectivity measurements on bulk and epitaxial GaSb. *Journal of Physics C* **13**, 2959–2968 (1980).

24. Katsidis, C. C. & Siapkas, D. I. General transfer-matrix method for optical multilayer systems with coherent, partially coherent, and incoherent interference. *Applied Optics* **41**, 3978–3987 (2002).

25. Haacke, G. New figure of merit for transparent conductors. *Journal of Applied Physics* **47**, 4086–4089 (1976).

26. Walsh, A. *et al.* Nature of the band gap of $In_2O_3$ revealed by first-principles calculations and x-ray spectroscopy. *Physical Review Letters* **100**, 167402 (2008).

27. Walsh, A., Da Silva, J. L. F. & Wei, S.-H. Origins of band-gap renormalization in degenerately doped semiconductors. *Physical Review B* **78**, 075211 (2008).

28. Zawadzki, W. & Szymańska, W. Elastic electron scattering in InSb-type semiconductors. *Physica Status Solidi (b)* **45**, 415–432 (1971).

29. Zawadzki, W. Mechanisms of Electron Scattering in Semiconductors. In *Handbook of Semiconductors*, chap. 12, 713–803 (North-Holland, 1982).

30. Pisarkiewicz, T. & Kolodziej, A. Nonparabolicity of the conduction band structure in degenerate tin dioxide. *Physica Status Solidi (B)* **158**, K5–K8 (1990).

31. Whittles, T. J. *et al.* Band Alignments, Valence Bands, and Core Levels in the Tin Sulfides SnS, $SnS_2$, and $Sn_2S_3$: Experiment and Theory. *Chemistry of Materials* **28**, 3718–3726 (2016).

32. Körber, C. *et al.* Electronic structure of $In_2O_3$ and Sn-doped $In_2O_3$ by hard x-ray photoemission spectroscopy. *Physical Review B* **81**, 165207 (2010).

33. Swallow, J. E. N. *et al.* Self-compensation in transparent conducting F-doped $SnO_2$. *Advanced Functional Materials* **28**, 1701900 (2018).

34. Scanlon, D. O. *et al.* Theoretical and Experimental Study of the Electronic Structures of $MoO_3$ and $MoO_2$. *The Journal of Physical Chemistry C* **114**, 4636–4645 (2010).

35. Scofield, J. Theoretical photoionization cross sections from 1 to 1500 keV. Tech. Rep., Divison of Technical Information Extension, U.S. Atomic Energy Commission (1973).

36. Wahila, M. J. *et al.* Lone-Pair Stabilization in Transparent Amorphous Tin Oxides: A Potential Route to p-Type Conduction Pathways. *Chemistry of Materials* **28**, 4706–4713 (2016).

37. Sallis, S. *et al.* La-doped $BaSnO_3$—Degenerate perovskite transparent conducting oxide: Evidence from synchrotron x-ray spectroscopy. *Applied Physics Letters* **103**, 42105 (2013).

38. Kresse, G. & Hafner, J. Ab initio molecular-dynamics simulation of the liquid-metal–amorphous-semiconductor transition in germanium. *Physical Review B* **49**, 14251–14269 (1994).

39. Kresse, G. & Hafner, J. Ab initio molecular dynamics for liquid metals. *Physical Review B* **47**, 558–561 (1993).

40. Kresse, G. & Furthmüller, J. Efficiency of ab-initio total energy calculations for metals and semiconductors using a plane-wave basis set. *Computational Materials Science* **6**, 15–50 (1996).

41. Kresse, G. & Furthmüller, J. Efficient iterative schemes for ab initio total-energy calculations using a plane-wave basis set. *Physical Review B* **54**, 11169–11186 (1996).

42. Blöchl, P. E. Projector augmented-wave method. *Physical Review B* **50**, 17953–17979 (1994).

43. Heyd, J., Scuseria, G. E. & Ernzerhof, M. Hybrid functionals based on a screened coulomb potential. *The Journal of Chemical Physics* **118**, 8207–8215 (2003).

44. Paier, J. *et al.* Screened hybrid density functionals applied to solids. *The Journal of Chemical Physics* **124**, 154709 (2006).

45. Ramzan, M., Li, Y. & Ahuja, R. Electronic structure, mechanical and optical properties of $In_2O_3$ with hybrid density functional (HSE06). *Solid State Communications* **172**, 37–40 (2013).

46. Walsh, A., Da Silva, J. L. F., Yan, Y., Al-Jassim, M. M. & Wei, S.-H. Origin of electronic and optical trends in ternary $In_2O_3(ZnO)_n$ transparent conducting oxides (n=1,3,5): Hybrid density functional theory calculations. *Physical Review B* **79**, 073105 (2009).

47. Walsh, A. & Scanlon, D. O. Polymorphism of indium oxide: Materials physics of orthorhombic $In_2O_3$. *Physical Review B* **88**, 161201 (2013).

48. Ágoston, P., Albe, K., Nieminen, R. M. & Puska, M. J. Intrinsic n-type behavior in transparent conducting oxides: A comparative hybrid-functional study of $In_2O_3$, $SnO_2$, and ZnO. *Physical Review Letters* **103**, 245501 (2009).

49. Goyal, A., Gorai, P., Peng, H., Lany, S. & Stevanovic, V. A computational framework for automation of point defect calculations. *Computational Materials Science* **130**, 1–9 (2017).

50. Scanlon, D. O., Regoutz, A., Egdell, R. G., Morgan, D. J. & Watson, G. W. Band gap engineering of $In_2O_3$ by alloying with $Tl_2O_3$. *Applied Physics Letters* **103**, 262108 (2013).

51. Regoutz, A. *et al.* Electronic and surface properties of Ga-doped $In_2O_3$ ceramics. *Applied Surface Science* **349**, 970–982 (2015).

52. Chase, M. W. *J. Phys. Chem. Ref. Data Monogr. No. 9 NIST. JANAF Thermochem. Tables* **9**, 1 (1998).

53. Dixon, S. C. *et al.* Transparent conducting n-type ZnO:Sc – synthesis, optoelectronic properties and theoretical insight. *Journal of Materials Chemistry C* **5**, 7585–7597 (2017).

54. Van de Walle, C. G. & Neugebauer, J. First-principles calculations for defects and impurities: Applications to III-nitrides. *Journal of Applied Physics* **95**, 3851–3879 (2004).

55. Lany, S. & Zunger, A. Assessment of correction methods for the band-gap problem and for finite-size effects in supercell defect calculations: Case studies for ZnO and GaAs. *Physical Review B* **78**, 235104 (2008).

56. Nieminen, R. M. Issues in first-principles calculations for defects in semiconductors and oxides. *Modelling and Simulation in Materials Science and Engineering* **17**, 084001 (2009).

57. Hine, N. D. M., Frensch, K., Foulkes, W. M. C. & Finnis, M. W. Supercell size scaling of density functional theory formation energies of charged defects. *Physical Review B* **79**, 024112 (2009).

58. Murphy, S. T. & Hine, N. D. M. Anisotropic charge screening and supercell size convergence of defect formation energies. *Physical Review B* **87**, 094111 (2013).

59. Persson, C., Zhao, Y.-J., Lany, S. & Zunger, A. n-type doping of $CuInSe_2$ and $CuGaSe_2$. *Physical Review B* **72**, 035211 (2005).

60. Cordfunke, E., Konings, R. & Ouweltjes, W. The standard enthalpy of formation of $In_2O_3$. *The Journal of Chemical Thermodynamics* **23**, 451–454 (1991).

61. Popescu, V. & Zunger, A. Extracting E versus k effective band structure from supercell calculations on alloys and impurities. *Physical Review B* **85**, 085201 (2012).

62. Medeiros, P. V. C., Stafström, S. & Björk, J. Effects of extrinsic and intrinsic perturbations on the electronic structure of graphene: Retaining an effective primitive cell band structure by band unfolding. *Physical Review B* **89**, 041407 (2014).

63. Medeiros, P. V. C., Tsirkin, S. S., Stafström, S. & Björk, J. Unfolding spinor wave functions and expectation values of general operators: Introducing the unfolding-density operator. *Physical Review B* **91**, 041116 (2015).

64. Ágoston, P. *et al.* Limits for n-type doping in $In_2O_3$ and $SnO_2$: A theoretical approach by first-principles calculations using hybrid-functional methodology. *Journal of Applied Physics* **108**, 053511 (2010).

65. Marezio, M. Refinement of the crystal structure of $In_2O_3$ at two wavelengths. *Acta Crystallographica* **20**, 723–728 (1966).

66. Weiher, R. L. & Ley, R. P. Optical properties of indium oxide. *Journal of Applied Physics* **37**, 299–302 (1966).

67. Janowitz, C. *et al.* Experimental electronic structure of $In_2O_3$ and $Ga_2O_3$. *New Journal of Physics* **13**, 085014 (2011).

68. Preissler, N., Bierwagen, O., Ramu, A. T. & Speck, J. S. Electrical transport, electrothermal transport, and effective electron mass in single-crystalline $In_2O_3$ films. *Physical Review B* **88**, 085305 (2013).

69. Fuchs, F. & Bechstedt, F. Indium-oxide polymorphs from first principles: Quasiparticle electronic states. *Physical Review B* **77**, 155107 (2008).

70. Scherer, V. *et al.* Transport and angular resolved photoemission measurements of the electronic properties of $In_2O_3$ bulk single crystals. *Applied Physics Letters* **100**, 212108 (2012).

71. Feneberg, M. *et al.* Many-electron effects on the dielectric function of cubic $In_2O_3$: Effective electron mass, band nonparabolicity, band gap renormalization, and Burstein-Moss shift. *Physical Review B* **93**, 045203 (2016).

72. King, P. D. C. *et al.* Band gap, electronic structure, and surface electron accumulation of cubic and rhombohedral $In_2O_3$. *Physical Review B* **79**, 205211 (2009).

73. Zhang, K. H. *et al.* Microscopic origin of electron accumulation in $In_2O_3$. *Physical Review Letters* **110**, 056803 (2013).

74. Frodason, Y. K., Johansen, K. M., Bjørheim, T. S., Svensson, B. G. & Alkauskas, A. Zn vacancy as a polaronic hole trap in ZnO. *Physical Review B* **95**, 094105 (2017).

75. Reunchan, P., Zhou, X., Limpijumnong, S., Janotti, A. & Van de Walle, C. G. Vacancy defects in indium oxide: An ab-initio study. *Current Applied Physics* **11**, S296–S300 (2011).

76. Scanlon, D. O. & Watson, G. W. On the possibility of p-type $SnO_2$. *Journal of Materials Chemistry* **22**, 25236 (2012).

77. Scanlon, D. O. Defect engineering of $BaSnO_3$ for high-performance transparent conducting oxide applications. *Physical Review B* **87**, 161201 (2013).

78. Xu, J. *et al.* Design of n-type transparent conducting oxides: The case of transition metal doping in $In_2O_3$. *Advanced Electronic Materials* **4**, 1700553 (2018).

79. González, G. B. Investigating the defect structures in transparent conducting oxides using x-ray and neutron scattering techniques. *Materials* **5**, 818–850 (2012).

80. Nadaud, N., Lequeux, N., Nanot, M., Jové, J. & Roisnel, T. Structural studies of tin-doped indium oxide (ITO) and $In_4Sn_3O_{12}$. *Journal of Solid State Chemistry* **135**, 140–148 (1998).